AIAA 80-1331R

Computations of the Oblique Impingement of Round Jets upon a Plane Wall

A. Rubel*
Grumman Aerospace Corporation, Bethpage, N. Y.

An inviscid, rotational flow model for incompressible jet impingement is formulated in terms of vector and scalar potentials and the vector vorticity. The set of four elliptic partial-differential equations governing the kinematics of the flow and three coupled hyperbolic equations for the vorticity are solved numerically for the impingement of fully developed round jets upon a plane wall at incidence angles of 90 (normal), 75, and 60 deg. The finite-difference computations are consistent with both existing rotational stagnation point analysis and reported data on stagnation point location, wall pressure, and, to a lesser extent, azimuthal distribution of momentum efflux.

Introduction

THE oblique impingement of a fully developed round jet upon a plane wall establishes a three-dimensional flowfield with properties of some relevance to the analysis of VTOL aircraft in ground effect. Application of integral conservation (i.e., control volume) laws to the system provides global constraints on the flow behavior but only a detailed flowfield analysis can determine the azimuthal distribution of momentum efflux.[1] To date, researchers requiring such information[2,3] have employed the data of Donaldson and Snedeker[4,5] whose observations are unique to the literature. The results of a theoretical/numerical study of incompressible inviscid, rotational round jet impingement at incidence angles in the 60-90 deg range complement this data set and are presented here.

The inviscid, rotational flow model has successfully resolved a variety of jet impingement problems where the vorticity (vorticity/radius) is conserved, or "frozen," on two-dimensional (axisymmetric) stream surfaces.[6] Hence, once the vorticity function is specified in terms of the stream function (e.g., via jet influx conditions) it is known throughout the flowfield. The oblique impingement of a round jet, on the other hand, creates a fully three-dimensional flowfield for which a stream function formulation is inapplicable. Furthermore, the inviscid rotational flow description no longer implies that vorticity is "frozen" along streamlines and an alternative solution technique is required. A vector potential/vorticity formulation for this problem has been given[7,8] and validated by computations of axisymmetric jet normal impingement within a three-dimensional Cartesian coordinate framework.[8] This approach separates the representation of the flowfield into two sets of coupled partial-differential equations. The first set, determined by the kinematics of the flow, is elliptic in nature and describes the velocity field in terms of vector and scalar potentials when the vorticity field is specified. The second set, determined by the inviscid rotational flow model, is hyperbolic and describes the behavior of the vorticity for a given velocity field. This technique for splitting the flowfield has been formulated by Hirasaki and Hellums[9] and Richardson and Cornish[10] for viscous flows where the velocity normal to the surface bounding the domain of integration is specified. Finite-difference solutions, within the context of this formulation, have been accomplished for enclosed flow[11,12] and, more recently, for open flow[13,14] systems.

The modified formulation[8] incorporating notions of inviscid rotational flow and parallel efflux boundary conditions is reviewed next. Finite-difference solution techniques and computational results are discussed subsequently.

Formulation

A Cartesian coordinate system with origin at the intersection of the jet centerline with the ground plane is used to describe the impingement flowfield (Fig. 1). Although the jet is considered to have a lateral plane of symmetry ($y=0$), this involves no loss in generality for the overall formulation of the problem. The boundaries of the impingement regime are such that the influx plane ($z=Z$) is unaffected by the presence of the ground plane ($z=0$), and the efflux planes ($x=X_-$, X_+; $y=Y$) are sufficiently distant from the stagnation point that the flow has recovered to the ambient pressure of the influx plane. The flow model implies that the impingement zone is a regime where the pressure and inertia forces are balanced so that the velocity-vorticity distribution at the influx plane, along with the assumption of parallel flow at the efflux plane, determines the fluid behavior within the zone.

The formulation is given in terms of dimensionless quantities; velocities are scaled by the maximum jet velocity, distance by the jet half-width (i.e., distance measured along the perpendicular from the jet centerline to the point at which velocity is half the maximum), and pressures by the total pressure at the jet centerline. Ambient and jet static pressures are taken to be zero.

Within the impingement zone the velocity vector $\bar{q}$ may be represented by a scalar potential ϕ and a vector potential $\bar{A}$ so that

$$\bar{q}=-\nabla\phi+\nabla\times\bar{A} \tag{1}$$

Here $\bar{A}$ is defined such that

$$\nabla\cdot\bar{A}=0 \tag{2}$$

which, along with the curl of velocity definition of vorticity $\bar{\omega}$ demands that

$$\nabla^2\bar{A}=-\bar{\omega} \tag{3}$$

Continuity is ensured by requiring that

$$\nabla^2\phi=0 \tag{4}$$

Presented as Paper 80-1331 at the AIAA 13th Fluid and Plasma Dynamics Conference, Snowmass, Colo., July 14-16, 1980; submitted Aug. 25, 1980; revision received Feb. 2, 1981.

*Head, Theoretical Aerodynamics Laboratory, Research Department. Member AIAA.

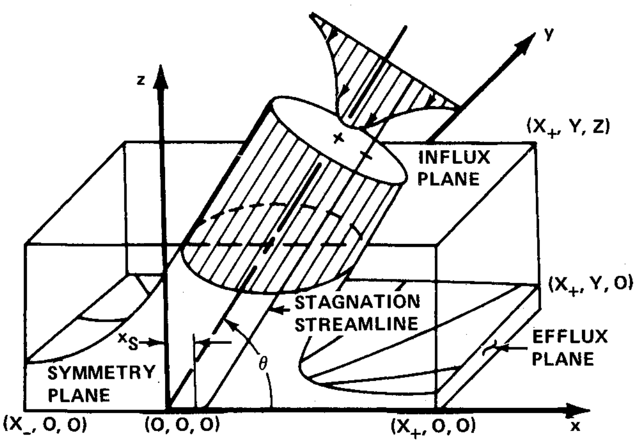

Fig. 1 Jet impingement zone and coordinate system.

The x, y, z scalar components of the vector fields are given by

$$\bar{q} = (u,v,w), \qquad \bar{A} = (\alpha,\beta,\gamma), \qquad \bar{\omega} = (\xi,\eta,\zeta)$$

Hirasaki and Hellums[9] have demonstrated and Richardson and Cornish[10] have confirmed that the boundary conditions

$$A_{(t)} = \frac{\partial A_{(n)}}{\partial n} = 0 \tag{5a,b}$$

$$\frac{\partial \phi}{\partial n} = -\bar{n}\cdot\bar{q} \tag{5c}$$

are such that Eqs. (3) and (4), subject to the auxiliary Eq. (2), can be satisfied, and the velocity normal to the bounding planes can be prescribed. Here the subscripts (n) and (t), indicate normal and tangential components, respectively, and $\bar{n}$ indicates the outward positive normal to the boundary. The velocity components normal to the bounding efflux planes are unknown for the impingement zone, and some alternative specification is required upon these surfaces. The condition of parallel outflow necessitates that the vertical velocity vanishes, or

$$\phi_z = \beta_x - \alpha_y \tag{5d}$$

at these efflux planes, where the subscripts denote the appropriate differentiation, and this completes the kinematic formulation.

The vorticity forcing functions introduced in Eq. (3) must be evaluated in concert with the scalar and vector potentials. The equation governing the behavior of vorticity is obtained from the curl of the momentum equation. For an inviscid fluid the resulting Helmholtz equation has the incompressible form

$$\bar{q}\cdot\nabla\bar{\omega} - \bar{\omega}\cdot\nabla\bar{q} = 0 \tag{6}$$

from which it may be shown (e.g., Milne-Thomson,[15] Aris[16]) that vortex lines are material lines. Furthermore, the envelope of vortex lines containing fixed material forms a Lamb surface[16] on which the total pressure is constant and governed by the Bernoulli equation,

$$\nabla(p+q^2) = 2(\bar{q}\times\bar{\omega}) \tag{7}$$

The hyperbolic nature of Eq. (6) implies that if influx occurs only along the $z=Z$ plane and if there are no recirculation bubbles within the domain of integration, then specification of $\bar{\omega}(x,y,Z)$ is sufficient for the determination of the vorticity field.

Numerical Procedures

The formulation for the impingement problem produces a set of four scalar kinematic equations, namely,

$$\alpha_{xx} + \alpha_{yy} + \alpha_{zz} = -\xi \tag{8}$$

$$\beta_{xx} + \beta_{yy} + \beta_{zz} = -\eta \tag{9}$$

$$\gamma_{xx} + \gamma_{yy} + \gamma_{zz} = -\zeta \tag{10}$$

$$\phi_{xx} + \phi_{yy} + \phi_{zz} = 0 \tag{11}$$

with boundary conditions

$$x = X_-, X_+ \ ; \ \alpha_x = 0,\ \beta = 0,\ \gamma = 0,\ \phi_z = \beta_x - \alpha_y \tag{12a,b}$$

$$y = 0 \ ; \ \alpha = 0,\ \beta_y = 0,\ \gamma = 0,\ \phi_y = 0 \tag{12c}$$

$$y = Y \ ; \ \alpha = 0,\ \beta_y = 0,\ \gamma = 0,\ \phi_z = \beta_x - \alpha_y \tag{12d}$$

$$z = 0 \ ; \ \alpha = 0,\ \beta = 0,\ \gamma_z = 0,\ \phi_z = 0 \tag{12e}$$

$$z = Z \ ; \ \alpha = 0,\ \beta = 0,\ \gamma_z = 0,\ \phi_z = -w(x,y,Z) \tag{12f}$$

The velocity profile above the influx plane (i.e., $z \geq Z$) is assumed to be undisturbed and fully developed[17] so that the normal velocity boundary condition Eq. (12f) is

$$w(x,y,Z) = -\sin\theta / [1 + kr^2(Z)]^2 \qquad k = \sqrt{2} - 1 \tag{13}$$

where θ is the jet incidence angle (Fig. 1) and $r(Z)$ is defined as the distance along the perpendicular, from points within the influx plane, to the jet centerline,

$$r^2(Z) = (x\sin\theta - Z\cos\theta)^2 + y^2 \tag{14}$$

The three scalar vorticity equations are

$$u\xi_x + v\xi_y + w\xi_z = u_x\xi + u_y\eta + u_z\zeta \tag{15}$$

$$u\eta_x + v\eta_y + w\eta_z = v_x\xi + v_y\eta + v_z\zeta \tag{16}$$

$$u\zeta_x + v\zeta_y + w\zeta_z = w_x\xi + w_y\eta + w_z\zeta \tag{17}$$

with influx conditions consistent with Eq. (13) and parallel inflow, that is

$$\left.\begin{aligned} \xi(x,y,Z) &= \Omega(Z)y\sin\theta \\ \eta(x,y,Z) &= -\Omega(Z)(x\sin\theta - Z\cos\theta) \\ \zeta(x,y,Z) &= -\Omega(Z)y\cos\theta \end{aligned}\right\} \tag{18a}$$

where

$$\Omega(Z) = 4k[1 + kr^2(Z)]^{-3}$$

and symmetry conditions given by

$$\xi(x,0,z) = \eta_y(x,0,z) = \zeta(x,0,z) = 0 \tag{18b}$$

Finite-difference techniques are employed in order to solve these governing equations. The numerical integration domain makes use of a uniform mesh system with spacing defined by

$$\Delta x = (X_+ - X_-)/(N_X - 1)$$

$$\Delta y = Y/(N_Y - 1), \quad \Delta z = Z/(N_Z - 1)$$

where N_X, N_Y, and N_Z are the number of points in the x, y, and z directions, respectively. Straightforward central-differencing about interior points is used to transform the elliptic Eqs. (8-11) to their second-order accurate numerical equivalents. Fictitious points are added to satisfy the normal derivative boundary conditions, Eqs. (12a-f). The value of the scalar potential on the efflux planes is evaluated by integration of the parallel outflow requirements Eqs. (12a, b, and d), from the $z=Z$ plane to the ground. Values of ϕ along the efflux edges of the $z=Z$ plane are assigned by choosing

$\phi(X_-,0,Z)=0$ and integrating the equations resulting from the stipulation that the velocity directed along these edges vanish, that is, $\phi_y=\alpha_z-\gamma_x$ on $x=X_-$, X_+ and $\phi_x=\gamma_y-\beta_z$ on $y=Y$.

Integration of the hyperbolic system, Eqs. (15-17) takes place on the existing grid network. Each vorticity derivative is represented by a three-point windward difference; all coefficients and the forcing terms are centered about the point in question. Since the flow is always directed toward the wall and away from the symmetry plane this amounts to backward-differencing y and z direction vorticity derivatives and requires monitoring only the u component of velocity for the upstream determination. The result is a set of second-order accurate implicit-difference equations which couple the three components of vorticity, at each grid point, within planes parallel to the wall. Equation (18a) is used to evaluate $\bar{\omega}(x,y,Z)$ and $\bar{\omega}(x,y,Z-\Delta z)$, the starting data on two planes, required to solve the system via a marching procedure.

The overall iteration procedure begins by setting the potential fields to zero and initializing the vorticity field by

$$\xi(x,y,z)=\Omega(z)y\sin\theta$$

$$\eta(x,y,z)=-\Omega(z)\,(x\sin\theta-z\cos\theta)$$

$$\zeta(x,y,z)=\zeta(x,y,Z-\Delta z)z/(Z-\Delta z)$$

where

$$\Omega(z)=4k[1+kr^2(z)]^{-3};\qquad z\geq r(z)/2$$

$$\Omega(z)=4k[1+2kzr(z)]^{-3};\qquad z<r(z)/2$$

The multigrid (MG) technique of Brandt[18] is employed, with line relaxation sweeps, to resolve the difference equations for β, α, γ, ϕ, in that order, until each residual[18] has a value less than 5×10^{-4}. The MG approach takes advantage of the relaxation technique's ability to correct short wavelength errors within a few iterations and relies on coarse grid smoothing to correct the larger wavelength errors. The coarse grid computations, here performed on grids with mesh widths in multiples of two, take a minimum of computer time compared with the three-dimensional fine mesh calculations. Use of this scheme improved convergence times by about a factor of five over standard optimized SLOR techniques when applied to the current set of elliptic equations. It should be noted that if the velocity normal to the efflux plane were known then Eq. (11) would require only a one-time solution. Here, however, conditions Eqs. (12a, b, and c) require that the calculation of ϕ be incorporated within the overall iteration scheme making use of the latest vector potential values.

Next, numerical solutions to Eqs. (15-17) are effected by marching in Δz increments to within one mesh width of the wall. At each interval, the three quasi-two-dimensional difference equations are iterated upon via line relaxation, sweeping from the symmetry plane toward the efflux plane, $y=Y$. Tolerances, based upon vorticity change per iteration, normalized by the field maxima, are only 10^{-2} initially. This entire potential/vorticity solution procedure is repeated until the vorticity system is converged, at the last plane, in a single sweep. At this point the tolerance on the vorticity computation is reduced by half an order of magnitude and the processes repeated until the desired final tolerance level is achieved.

This overall procedure provides convergence in from 40 to 140 steps for a tolerance of 10^{-5} on vorticity. The intermediate convergence of vorticity at less restrictive tolerances, as well as use of under-relaxation factors in the 0.1-0.3 range, prove necessary to avoid divergence of the calculation. The computations reported here utilize a $(33\times17\times49)$ grid and require IBM 370-168 running times of from 1 to 2 h for impingement incidence angles in the 90-60 deg range, respectively. Many numerical experiments, carried out on a more coarse $(25\times13\times25)$ grid, indicate that adequate results can be achieved with 15 min running times.

Upon convergence, the determination of wall velocities requires the numerical evaluation of Eq. (1), viz.,

$$u=-\phi_x+\gamma_y-\beta_z,\qquad v=-\phi_y+\alpha_z-\gamma_x \qquad (19a,b)$$

Normal impingement computations, using centered differences for γ_y and γ_x, indicate that, for the mesh widths used here, second-order windward differencing of ϕ_x and ϕ_y, especially near the efflux edges, provides more accurate profiles than center-differencing these terms. Furthermore, the normal derivatives β_z, α_z are best evaluated from second-order Taylor series expansions in z involving the potentials at a distance Δz from the wall and Eqs. (8) and (9) to extract

$$\alpha_{zz}(x,y,0)=-\xi(x,y,0)$$

$$\beta_{zz}(x,y,0)=-\eta(x,y,0) \qquad (20)$$

A central-differenced representation of Eqs. (15) and (16) about points a mesh height above the ground[8] is used, with $\zeta(x,y,0)=0$, to extrapolate ξ and η to the wall.

Fully-developed jet impingement normal to the wall produces a stagnation line with zero vorticity. When the jet is inclined the stagnation line is shifted (Fig. 1) and, as a consequence, becomes rotational. Hayes[19] has shown that, in the vicinity of a nearly axisymmetric rotational stagnation region, the vorticity exhibits, approximately, a $z^{-1/2}$ behavior. Strictly speaking then, use of Eq. (20) is no longer valid and a standard three-point one-sided formulation for the evaluation of α_z and β_z could be implemented. In practice, the two methods yield numerical results which differ by no more than 10% over the range of computations presented herein and the vorticity extrapolation technique is used throughout. A similar Taylor expansion procedure is used to evaluate β_x at $x=X_-$, X_+ and α_y at $y=Y$ for satisfaction of the parallel efflux conditions. Here, of course, the vorticities are well behaved.

Results and Discussion

Three cases of oblique jet impingement were selected for numerical solution upon the $(33\times17\times49)$ grid system (Table 1). The results of these computations correspond to the observations of Donaldson and Snedeker[4,5] for large values of height above ground to jet diameter (i.e., $h/d>7$) and subsonic jet Mach number $M=0.57$. Before performing a comparison of the present calculations with these data, it is instructive to examine the structure of the inviscid rotational impact region.

Vortex line traces on stream surfaces are used to illustrate the characteristics of the normal and oblique ($\theta=60$ deg) impingement flowfields (Fig. 2). These vortex tubes are generated by a three-step procedure. First, a symmetry plane streamline, initially parallel to the jet axis and at a distance $-r(Z)$ from it, is traced through the computational domain. Next, starting at the point of influx (i.e., $z=Z$), and for equal time intervals, successive vortex lines are traced from this streamline to the point of re-entrance into the symmetry plane. Finally, a second streamline, passing through the intersection of the topmost vortex line with the symmetry

Table 1 Domain for numerical integration

θ, deg	X_-	X_+	Y	Z
90	−4.0	4.0	4.0	2.2
75	−4.0	4.0	4.0	2.2
60	−4.5	4.0	3.5	2.1

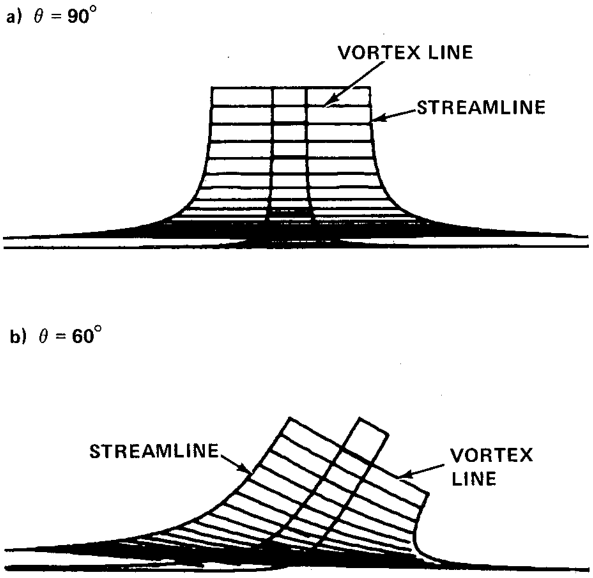

Fig. 2 Computed vortex tubes, $r(Z) = 0.2, 1.0$.

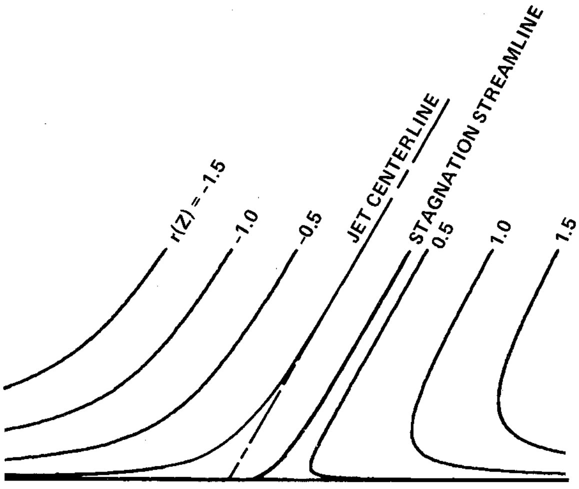

Fig. 3 Computed symmetry plane streamlines, $\theta = 60$ deg.

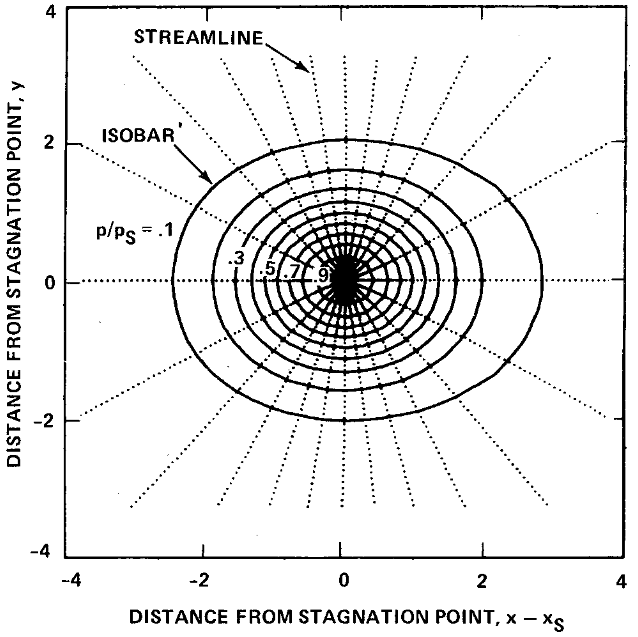

Fig. 4 Computed wall isobars and streamlines, $\theta = 60$ deg, $y < 0$ region generated via lateral symmetry.

plane, is traced through the impact field. This streamline, except for numerical inaccuracy, passes through each vortex line re-entry point on the symmetry plane. The view shown here (Fig. 2) is for a line of sight parallel to the y axis; the inner and outer vortex tubes were generated with $r(Z) = 0.2$ and 1.0, respectively.

The inviscid rotational vortex lines are material lines and here represent the history of rings of fluid originally centered about the jet axis. The oblique impingement fluid lines show bending in their approach to the wall in order to accommodate the ground condition,[19] $\zeta(x,y,0) = 0$, whereas the normal impingement vortex lines lie in planes parallel to the ground throughout the flowfield [i.e., $\zeta(x,y,z) = 0$]. Also, as the wall is approached, the increased density of vortex lines indicates the required reduction of normal velocity. This is particularly noticeable for the outer rings, since the fully-developed nature of the jet influx ensures that they are of lower energy than their inner ring counterparts. The central tube of high energy flow exits the impact region with azimuthal independence only when the jet impinges normally. Otherwise, the tube exhausts asymmetrically as part of an efflux momentum redistribution to maintain the balance with influx momentum.

More aspects of the oblique impingement flowfield are revealed by observing the streamline pattern within the symmetry plane for the $\theta = 60$ deg case (Fig. 3). Shown here are the stagnation streamline and streamlines centered about the jet centerline in 0.5 half-width intervals [i.e., $\Delta r(Z) = 0.5$]. Apparent is the streamline compression associated with the lateral spread of the flow along the ground plane. Construction of the stagnation streamline is accomplished by tracing backward in time from the stagnation point. The stagnation streamline follows a trajectory parallel to and displaced from the jet centerline. As a consequence of this shift, and the fully-developed inflow, the stagnation pressure is reduced. In the vicinity of the stagnation point the stagnation line exhibits a deflection toward the jet centerline. This behavior differs from irrotational impingement, where the stagnation streamline enters normal to the wall, and differs from two-dimensional rotational impingement, where the stagnation streamline enters the wall virtually undeflected.[6]

To discuss the flow structure within the wall plane a polar coordinate system (R,σ) is defined where R is the radial distance from the stagnation point and σ is the azimuthal angle measured from the positive x axis. Streamlines are traced from starting points at $R = 0.01$ in equal angular increments, $\Delta\sigma = \pi/12$, and isobars are constructed from the Bernoulli equation, namely,

$$p = p_S - u^2 - v^2$$

for the $\theta = 60$ deg case (Fig. 4). Here, the subscript S refers to the stagnation point value and p_S is equated to the square of the maximum velocity computed in the wall plane. The isobars are close to circular in appearance and the streamlines possess a nearly radial, but certainly not symmetric, character with respect to the stagnation point. These features correspond to the near-axisymmetric rotational stagnation point analysis of Hayes,[19] where the classification parameter, defined by

$$\alpha_0 = [\,(v_y - u_x)/(v_y + u_x)\,]_S$$

has values $\alpha_0 = 0.03$ and 0.08 at $\theta = 75$ and 60 deg, respectively. The value $\alpha_0 = 0$ is associated with axisymmetric flow. The consequences of this behavior are that the velocity in the vicinity of the stagnation point behaves as

$$u(x_S, 0, z) \sim z^{(1-\alpha_0)/2} \tag{21}$$

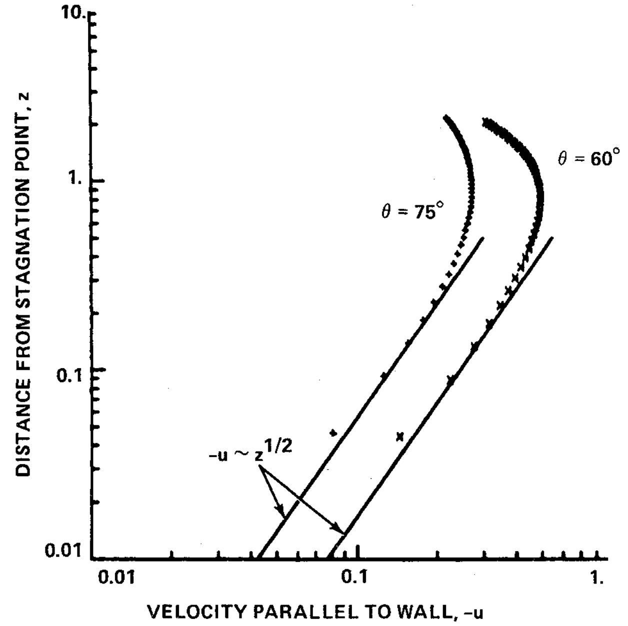

Fig. 5 Computed velocity distribution above the stagnation point.

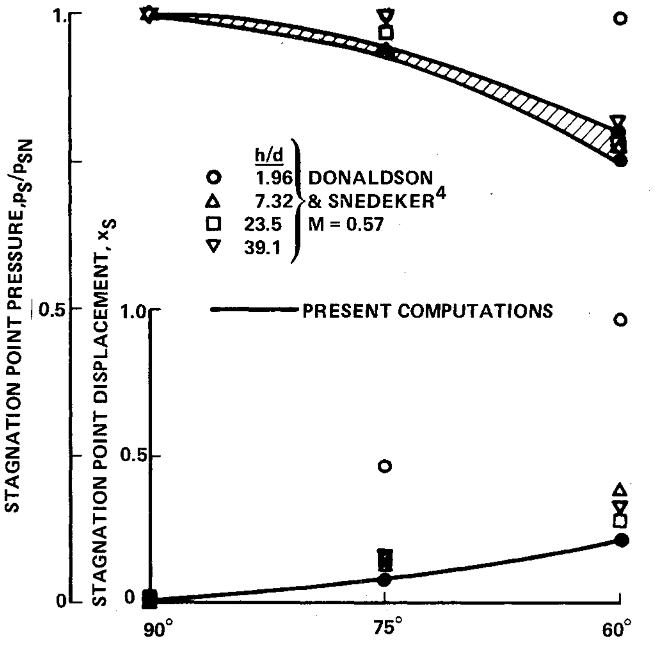

Fig. 6 Effect of impingement angle on stagnation point pressure and location.

the vorticity is infinite in the wall plane and the stagnation streamline enters the wall tangentially. Duplication of the tangential entry phenomenon is difficult to resolve numerically; however, the present results (Fig. 3) are consistent with such behavior. In addition, the velocity distribution computed in the vicinity of the stagnation point (Fig. 5) shows very good agreement with the theoretical description of Hayes [i.e., Eq. (21)].

The calculated incidence angle dependence of stagnation point location and stagnation pressure scaled by the normal impingement value p_{SN} are in reasonable agreement with data[4] for $h/d \gtrsim 7$ (Fig. 6). These fully-developed inflow results may be contrasted with the $h/d \simeq 2$ data where the influx velocity is essentially uniform. Here, the irrotational stagnation streamline bends away from the jet centerline, in order to enter the wall normally, and produces a large stagnation point displacement. Furthermore, the stagnation line evolves from a constant total pressure influx condition so that the stagnation pressure is unchanged with incidence angle.

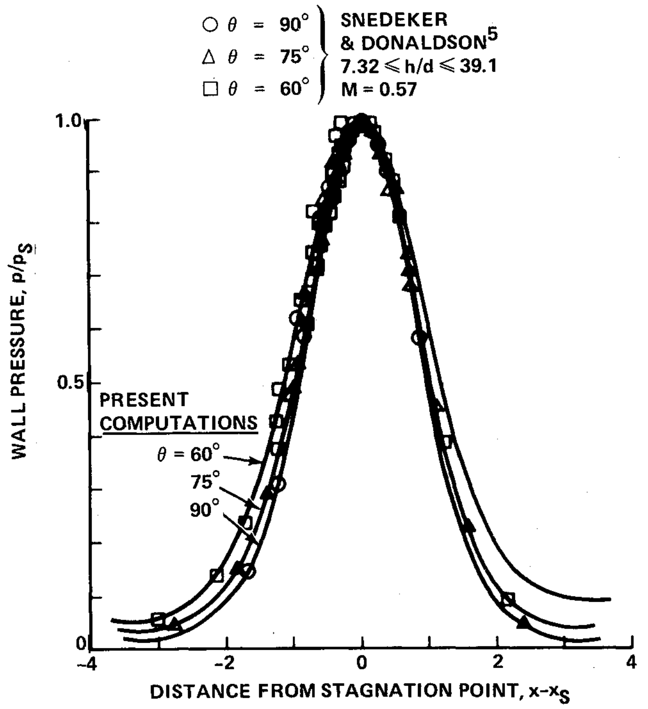

Fig. 7 Symmetry plane pressure distribution at the wall.

The shaded area (Fig. 6) denotes the range between alternative methods of extracting the stagnation pressure from the numerical solutions. The upper values are fixed from the stagnation streamline trace to the influx surface; the lower values from the maximum magnitude of the wall plane velocity. The two methods yield results different by 6% at $\theta = 60$ deg. Symmetry plane pressure distributions, calculated utilizing the latter technique, compare well with observations[5] (Fig. 7). These distributions are symmetric about the stagnation point and remarkably invariant in the $60 \leq \theta \leq 90$ deg range. The exception is some increased spreading predicted at the low pressure end of the $\theta = 60$ deg distribution, perhaps due to numerical limitations. If the azimuthal pressure distributions are nearly coincident then, from momentum considerations, $p_S \simeq p_{SN} \sin\theta$, a not unreasonable description of the data over the $60 \leq \theta \leq 90$ deg range of incidence. This behavior cannot be expected for the uniform influx condition (i.e., $h/d \sim 2$) where the pressure distribution is quite asymmetric.[4] Interestingly, the symmetry plane pressure distributions and stagnation point location characteristics presented here are very much analogous to previously reported two-dimensional results.[6]

The azimuthal distribution of the radial velocity, $q_{(R)}(3.281, \sigma, z)$, upon a cylindrical efflux surface exemplifies the three dimensionality of the oblique impingement flowfield (Figs. 8a-e). The profiles for $\theta = 60$ and 75 deg show progressive thickening as the azimuthal angle is increased from $\sigma = 0$ to $\sigma = \pi$ and, at $\sigma = \pi/2$, the profiles are coincident with the normal impingement result, except for a small region near the wall. The streamline of maximum energy, emanating from the jet centerline, is removed from the wall (Fig. 3) suggesting that, upon recovery of ambient pressure, the profile at $\sigma = \pi$ contains a velocity maximum. This peak is noted for the $\theta = 60$ deg case (Fig. 8e) and, in fact, the computed velocity is within 4% of the maximum value. The peak is more difficult to capture at $\theta = 75$ deg because the stagnation total pressure is quite close to the field maximum. The difference between the peak velocity and wall velocity

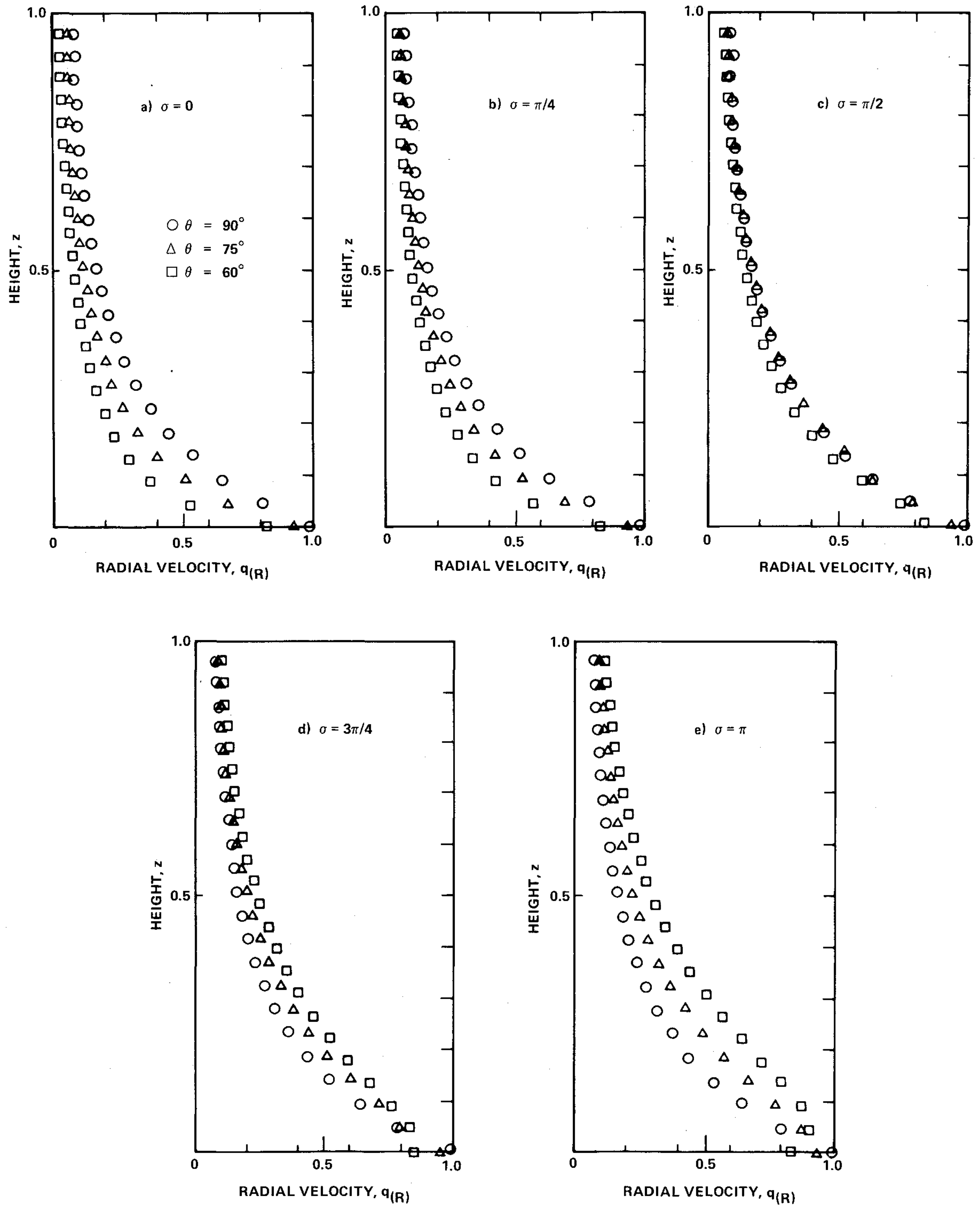

Fig. 8 Computed radial velocity profiles, $R = 3.281$.

diminishes with reduced azimuthal angle until it vanishes at $\sigma = 0$. The $\theta = 60$ deg velocity profile results at $\sigma = \pi/2$ and $3\pi/4$ (Figs. 8c and d) exhibit behavior indicative of a maximum velocity point within a mesh width of the wall plane. At $\sigma = \pi/4$ (Fig. 8b) evidence of the velocity maximum is no longer discernible. The corresponding azimuthal distribution of tangential velocity, i.e., $q_{(\sigma)}(3.281, \sigma, z)$, reveals maximum values located near the wall with values no greater than 0.1 (Figs. 9a-c). Thus, as per Donaldson and Snedeker[4,5] and Taylor[20] the efflux velocity is very nearly radial.

If the impingement flow is inviscid then Eq. (7) implies that each parcel of fluid which passes through the influx surface regains its kinetic energy when it emerges from the efflux surface, provided that the ambient pressure has been recovered. Thus,

$$\iint_{\text{efflux}} q^m \bar{q}\cdot\bar{n}\,\mathrm{d}s + \iint_{\text{influx}} q^m \bar{q}\cdot\bar{n}\,\mathrm{d}S = 0 \tag{22}$$

for an incompressible flow, where q is the magnitude of the velocity and $\mathrm{d}S$ is the dimensionless differential surface area.

Conservation of mass and energy are obtained from Eq. (22) with $m = 0$ and 2, respectively. The case of $m = 1$ is of particular interest since, from Eq. (13),

$$I = \iint_{\text{influx}} q\bar{q}\cdot\bar{n}\,\mathrm{d}S = -\pi/6k \tag{23}$$

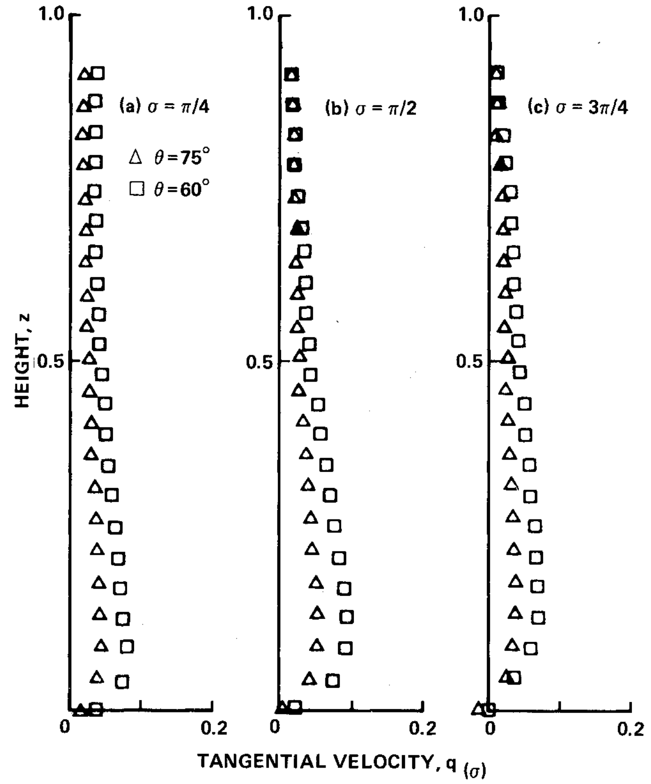

Fig. 9 Computed tangential velocity profiles, $R = 3.281$.

where $-I$ is half the magnitude of the fully-developed jet momentum. If the efflux is radial with respect to the stagnation point then the total momentum flux is

$$\iint_{\text{efflux}} q\bar{q}\cdot\bar{n}\,\mathrm{d}S = \int_0^\pi \dot{E}_{(R)}\,\mathrm{d}\sigma \equiv E_{(R)} \tag{24}$$

where dimensionless momentum flux densitites (per radian) are defined, in general, by

$$\dot{E}_{(x)} = R\int_0^Z q_{(x)}q_{(R)}\,\mathrm{d}z \tag{25}$$

The subscripts in parentheses refer to component directions (e.g., $q_{(x)} = u$, $q_{(y)} = v$).

Radially spreading wall jets nearly conserve $\dot{E}_{(R)}$ over lengths for which the wall shear force is small vis-a-vis $\dot{E}_{(R)}$. Hence,

$$E_{(R)} + I = \epsilon \tag{26}$$

where ϵ is zero for the inviscid case and is expected to be small, over short distances, for real flows that become radial prior to appreciable entrainment. The integral constraint of Eq. (26), with $|\epsilon| \ll |I|$, does not preclude significant differences between real and inviscid velocity profiles (e.g., Siclari[2] and Taylor[20]).

In addition, the integral vector momentum laws require that

$$E_{(x)} = -I_{(x)} = I\cos\theta \tag{27}$$

$$F_{(z)} = -\iint_{\text{wall}} p(x,y,0)\,\mathrm{d}x\mathrm{d}y = -2I_{(z)} = 2I\sin\theta \tag{28}$$

$$F_{(y)} = -E_{(y)} \tag{29}$$

Table 2 Calculated integral momentum parameters

θ, deg	$-E_{(R)}/I$	$-E_{(x)}/I_{(x)}$	$-2I_{(z)}/F_{(z)}$	$(\pi/2)E_{(y)}/I_{(z)}$
90	1.014	-	0.946	1.017
75	0.992	0.882	0.892	1.006
60	0.954	0.871	0.825	1.015

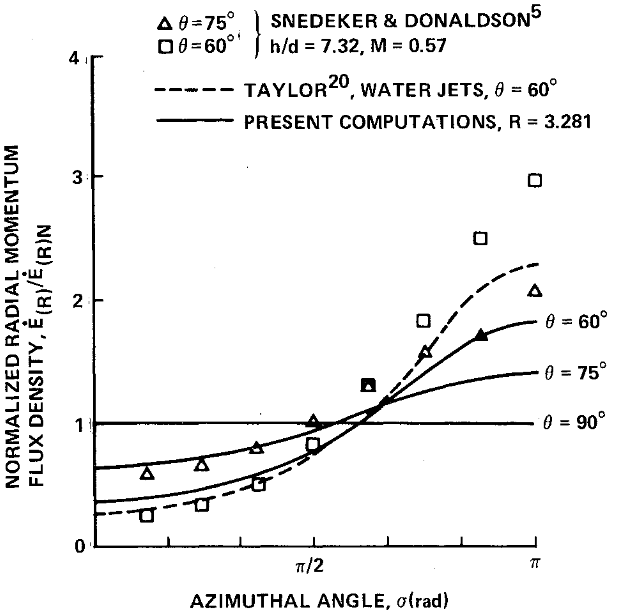

Fig. 10 Azimuthal distribution of radial momentum efflux.

where $F_{(y)}$, $F_{(z)}$ are the dimensionless forces exerted on the symmetry and ground planes, respectively.

The integral relationships Eqs. (26-29) provide a standard for evaluation of both computational results and test data. Numerical integration of each influx momentum component reveals errors of no more than 1% at $\theta = 75$ and 90 deg and 3% at $\theta = 60$ deg in comparison with the exact results from integrations using Eq. (13). The summary of computed integral balances between influx and efflux (Table 2) shows that Eq. (26), with $\epsilon = 0$, is satisfied with, at most, a 5% error. Discrepancies of the order 13% (only 7% if scaled by the value of I) appear in the $\bar{x}$ - momentum flux balance, Eq. (27). These errors are more than likely a result of mesh resolution; for a $(25 \times 13 \times 25)$ grid they are increased to order 20%. Since small errors in the recovery to ambient pressure (recall Fig. 7) can yield an appreciable excess force on the wall, Eq. (28) is subject to deviations up to 17% at $\theta = 60$ deg.

The ratio of symmetry plane to wall half-plane reaction forces is observed[20] to be

$$2F_{(y)}/F_{(z)} = E_{(y)}/I_{(z)} \simeq 2/\pi \tag{30}$$

for irrotational round jet impingement at incidence angles $90 \le \theta \le 30$ deg. Furthermore, the present computations indicate that this relationship remains valid for inviscid rotational round jets, at least over the range $90 \le \theta \le 60$ deg. To date there is no explanation for this behavior although, for any normally impinging inviscid axisymmetric jet, the efflux velocity is functionally related to the influx velocity via[6] $q_{(R)}(2Rz) = -w(r^2)$ which is sufficient to verify Eq. (30) for $\theta = 90$ deg.

Computed distributions of the radial momentum flux are scaled by their normal impingement values, $\dot{E}_{(R)_N}$, and compared with Snedeker and Donaldson's results[5] extracted from test data (Fig. 10). For $\theta = 60$ and 75 deg the deviations from the axisymmetric distribution are observed to be considerably greater than those calculated, especially in the region of largest momentum flux excess (i.e., $\sigma \simeq \pi$). In-

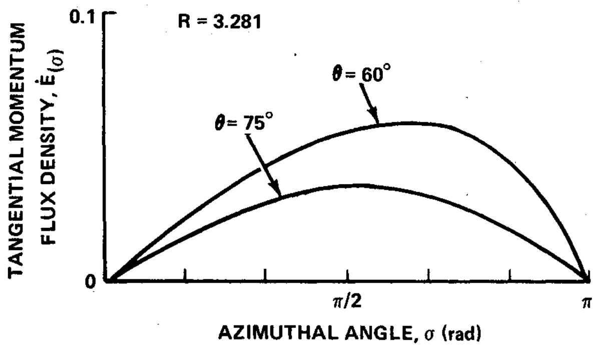

Fig. 11 Computed azimuthal distribution of tangential momentum efflux.

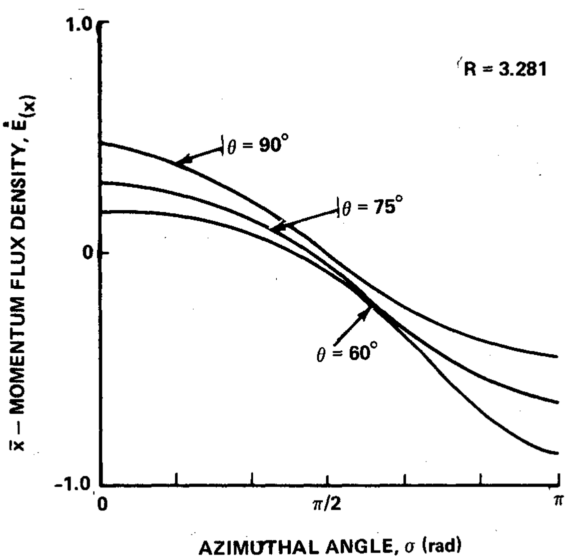

Fig. 12 Computed azimuthal distribution of $\bar{x}$-momentum efflux.

tegration of the experimentally determined distribution[5] yields total radial momentum fluxes in excess of $E_{(R)N}$ by 12-15% in comparison with the numerical result of a 5% deficiency. The apparent momentum flux surplus implied by the data[5] is illustrated by evaluation of $E_{(x)}/\pi\dot{E}_{(R)N}$ from the integration of

$$\dot{E}_{(x)}/\pi\dot{E}_{(R)N} \simeq \dot{E}_{(R)}\cos\sigma/\pi\dot{E}_{(R)N}$$

over the interval $0 \leq \sigma \leq \pi$. The result is found to exceed the theoretical value, cosθ, by 26% at $\theta = 75$ deg and 20% at $\theta = 60$ deg. The present computations are virtually invariant for $R \geq 3.281$ and underestimate the theoretical value by about half this amount. These results are placed in some perspective by viewing (Fig. 10) the direct measurements of momentum flux density obtained by Taylor[20] for the essentially irrotational oblique impingement of water jets. Calculations determine that this distribution, for $\theta = 60$ deg, is consistent with $E_{(R)N}$ and that $E_{(x)}$ satisfies the integral constraint of Eq. (27) to within 3%. Not surprisingly then, these data fall between the present computations and the results of Snedeker and Donaldson,[5] the chief uncertainties appearing in the $\sigma \geq 3\pi/4$ range.

The distribution of azimuthal momentum flux $\dot{E}_{(\sigma)}$ (Fig. 11) is in accordance with the tangential velocity profiles (Figs. 9a-c) with peak values occurring at increasing azimuth as θ is reduced. The tangential fluxes are small in comparison to the radial fluxes confirming the observation of radially spreading efflux.[4,5] As the jet incidence angle is reduced from normal the component of momentum flux density $\dot{E}_{(x)}$ is negatively displaced for all σ (Fig. 12). The greatest displacements are located near $\sigma \simeq 0$, π whereas the momentum flux at $\sigma \simeq \pi/2$ remains close to zero. This is consistent with the coincident radial velocity profiles at $\sigma = \pi/2$ (Fig. 8c). The lateral momentum flux has a distribution $\dot{E}_{(y)}$ that peaks at $\sigma = \pi/2$ for $\theta = 90$ deg and this peak advances in azimuth as the incidence angle is reduced (Fig. 13). The magnitude of the maximum drops such that the area under the distribution curve is proportional to sinθ.

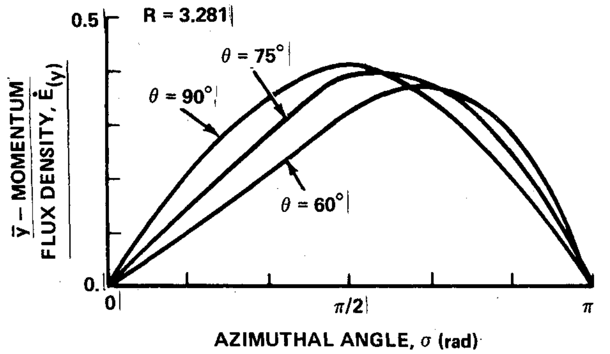

Fig. 13 Computed azimuthal distribution of lateral momentum efflux.

Conclusions

A vector potential/vorticity formulation for the oblique impingement of inviscid rotational jets upon a plane wall is given here. Finite-difference solutions of the governing equations are obtained for incompressible, fully developed jets at incidence angles $\theta = 60$, 75, and 90 deg. From a study of these results the following is concluded.

1) The computed inviscid rotational stagnation point behavior is consistent with the analysis of Hayes.[19]

2) Wall plane pressure distributions in the symmetry plane are very nearly independent of incidence angle, in close agreement with the experimental results of Snedeker and Donaldson.[5] The flowfield behavior in the symmetry plane closely resembles that of two-dimensional impingement.[6]

3) Forces on the symmetry plane and the wall half-plane are very nearly in the ratio $2/\pi$, independent of incidence angle. Taylor[20] has reported the same observation for irrotational round jet impingement.

4) Global momentum balances imply errors of up to 15% in the computations of the azimuthal distribution of momentum efflux. Inconsistencies of at least this order, but of opposing sign, are noted in the available data analysis.[5] Additional effort is necessary if the discrepancies between experimental and computational results are to be reconciled.

Acknowledgments

This investigation was partially supported by the Office of Naval Research, Contract N00014-77-C-0524. The author wishes to thank M. Siclari of the Research Department, Grumman Aerospace Corporation, for many helpful discussions.

References

[1] Taylor, G., "IV. Oblique Impact of a Jet on a Plane Surface," *Philosophical Transactions of The Royal Society (London)*, Vol. 260A, 1966, pp. 96-100.

[2] Siclari, M. J., Hill, W. G. Jr., and Jenkins, R. C., "Investigation of Stagnation Line and Upwash Formation," AIAA Paper 77-615, AIAA/NASA Ames V/STOL Conference, Palo Alto, Calif., June 1977.

[3] Kotansky, D. R. and Glaze, L. W., "Development of an Empirical Data Base and Analytical Modelling of Multi-Jet V/STOL Flow Fields in Ground Effect," *Proceedings of the V/STOL Aircraft Aerodynamics Conference,* Vol. I, Naval Postgraduate School, Monterey, Calif., May 16-18, 1979.

[4] Donaldson, C. du P. and Snedeker, R. S., "A Study of Free Jet Impingement. Part I, Mean Properties of Free and Impinging Jets," *Journal of Fluid Mechanics,* Vol. 45, 1971, pp. 281-319.

[5] Snedeker, R. S. and Donaldson, C. du P., "Experiments on the Oblique Impingement of Underexpanded Jets on a Flat Plate," A.R.A.P., Princeton, N. J., Rept. 64, April 1965.

[6] Rubel, A., "Computations of Jet Impingement on a Flat Surface," *AIAA Journal,* Vol. 18, Feb. 1980, pp. 168-175.

[7] Rubel, A., "Computational Techniques for the Calculation of Inviscid Rotational Impingement," AIAA Paper 78-1212, AIAA 11th Fluid and Plasma Dynamics Conference, Seattle, Wash., July 10-12, 1978.

[8] Rubel, A., "Computation of Inviscid Rotational Jet Impingement Regions," *Proceedings of the V/STOL Aircraft Aerodynamics Conference,* Vol. I, Naval Postgraduate School, Monterey, Calif., May 16-18, 1979.

[9] Hirasaki, G. J. and Hellums, J. D., "Boundary Conditions on the Vector and Scalar Potentials in Viscous Three-Dimensional Hydrodynamics," *Quarterly of Applied Mathematics,* Vol. 28, 1970, pp. 293-296.

[10] Richardson, S. M. and Cornish, A. R. H., "Solution of Three-Dimensional Incompressible Flow Problems," *Journal of Fluid Mechanics,* Vol. 82, 1977, pp. 309-319.

[11] Aziz, K. and Hellums, J. D., "Numerical Solution of the Three-Dimensional Equations of Motion for Laminar Natural Convection," *Physics of Fluids,* Vol. 10, 1967, pp. 314-324.

[12] Mallinson, G. D. and deVahl Davis, G., "Three-Dimensional Natural Convection in a Box: A Numerical Study," *Journal of Fluid Mechanics,* Vol. 83, 1977, pp. 1-31.

[13] Aregbesola, Y. A. S. and Burley, D. M., "The Vector and Scalar Potential Method for the Numerical Solution of Two- and Three-Dimensional Navier-Stokes Equations," *Journal of Computational Physics,* Vol. 24, 1977, pp. 398-415.

[14] Bower, W. W., Agarwal, R. K., and Peters, G. R., "A Theoretical Study of Two- and Three-Dimensional Impinging Jets," *Proceedings of the V/STOL Aircraft Aerodynamics Conference,* Vol. I, Naval Postgraduate School, Monterey, Calif., May 16-18, 1979.

[15] Milne-Thomson, L. M., *Theoretical Hydrodynamics,* 4th ed., The MacMillan Company, N. Y., 1960, pp. 83-85.

[16] Aris, R., *Vectors, Tensors, and the Basic Equations of Fluid Mechanics,* Prentice-Hall, Inc., N. J., 1962, pp. 96-97.

[17] Schlichting, H., *Boundary Layer Theory,* 4th ed., McGraw-Hill Book Company, Inc., N. Y., 1960, Chap. XXIII.

[18] Brandt, A., "Multi-Level Adaptive Solutions to Boundary-Value Problems," *Math of Comp.,* Vol. 31, 1977, pp. 333-390.

[19] Hayes, W. B., "Rotational Stagnation-Point Flow, *Journal of Fluid Mechanics,* Vol. 19, 1964, pp. 366-374.

[20] Taylor, G., "Formation of Thin Flat Sheets of Water," *Proceedings of the Royal Society A,* Vol. 259, 1960, pp. 1-17.